Correlation Analysis of the Hydrodynamic Characteristics and Stability of a Self-balancing Multistage Pump

W. S. Ma[1], D. W. Wang[2†], Y. B. Li[2], R. Cao[1] and Y. C. Yang[1]

[1] *Chongqing Pump Industry Co. Ltd. Chongqing, 400000, China*
[2] *School of Energy and Power Engineering, Lanzhou University of Technology, Lanzhou, Gansu Province, 730050, China*

†*Corresponding Author Email: 240944389@qq.com*

ABSTRACT

The BB5 series multistage centrifugal pump is commonly utilized for its capacity to deliver a large head. However, due to the long rotor system in the BB5 series multistage pump, the unsteady flow field structure of each impeller at every stage inevitably results in more complex mechanical characteristics of the pump, thereby affecting its operational stability. This paper conducts a numerical study on the stability of a 12-stage self-balancing multistage pump. The results indicated that significant pressure load fluctuations on the working surface occurred at the inlet of the impeller blades at all levels in the low-pressure section. At low flow conditions, the coincidence of the pressure loads on different blade working surfaces and back surfaces of the same impeller was poor; this resulted in an inadequate uniformity of the force distribution on each blade. A negative correlation was observed between the intensity of the pressure pulsation and the flow rate. In the inlet section the intensity of pressure fluctuation was stronger than that in the outlet section. The spectrum characteristic diagram of radial force shows that the frequencies with higher amplitudes occurring at each stage impeller are approximately 298 Hz and 48 Hz. The cause is the interference between the impeller blades and the guide vanes. At low flow rates, the amplitude of the radial force of the impeller was significantly higher than that at other flow rates. The magnitude of the residual axial force fluctuated to a certain degree, but its direction remained unchanged. The stability of the flow field and mechanical performance were inferior at low flow rates. At the same flow rate, the stability of the inlet section was worse. These research results could provide references for the stability design and optimization of self-balancing multistage pumps.

1. INTRODUCTION

The multistage pump can achieve a higher head through a series combination of two impellers. As an important power device, they have wide applications in agriculture and industry (Yuan et al., 2014; Lu et al., 2018; Milovančević et al., 2018; Wang et al., 2018). The BB5 series pumps are horizontal, double-casing constructions with a pressure bearing capacity exceeding 42.0 MPa at room temperature and a maximum allowable operating temperature over 400°C. This series is used mainly for transporting petroleum, refined oil, liquefied petroleum gas, boiler feed water and other clean, flammable, explosive and toxic media; these toxic media include the heavy oil hydrogenation feed pump of the oil refinery, the descaling pump of the steel plant and the boiler feed pump of the power plant.

At present, research on multistage pumps has focused mainly on the optimization of hydraulic performance. Zhao et al. (2023) used a multi-island genetic algorithm (MIGA) to optimize the hydraulic efficiency of a multistage pump at rated operating conditions. Jiang and Peng et al. found the optimal parameter combination to improve the efficiency of the design points using the response surface method (Jiang et al., 2021; Peng et al., 2021). Wu et al. (2023) introduced a multiobjective optimization approach for guide vanes utilizing an artificial neural network (NN) and a genetic algorithm (GA). Zhang et al. (2024) found that the impeller outlet width, blade wrap angle, guide vane inlet width, and other structural parameters are key factors affecting the hydraulic efficiency of multistage pumps. Kim et al. (2017) and Wang et al. (2023) performed numerical analyses to examine the impact of guide vane shape and

diameter affect pump performance characteristics. Isametova & Abilezova (2022) conducted experiments to study the relationship between the number of blades and the energy characteristics of multistage pumps, and a matching relationship between them was obtained. The focus of the aforementioned study is on how to improve the performance of multistage pumps. However, there is limited consideration of the relationship between the flow field and the stability of multistage pumps. The extremely high pressure and complex structure of multistage pumps inevitably have a significant impact on their stability. Many scholars have researched the stability of pump operation. Bai et al. studied the vibration characteristics of a multistage centrifugal pump and discovered that the primary frequency of vibration matched both the blade passing frequency and twice the blade passing frequency (Bai et al., 2019). Zhang et al. (2022) found that the vibration frequency of multi-stage pump bearings and the pump body is related to the shaft passing frequency (SPF) and the blade passing frequency (BPF). Al Tobi et al. (2017) analyzed and obtained the vibration mode of a centrifugal pump using an automatic diagnosis method. However, the operational stability of multistage pumps is influenced by various factors, including structural characteristics, rotor imbalance, unsteady excitation forces, and rotor instability during operation (Li et al., 2016; Zhang et al., 2018). The primary internal cause of issues in operating multistage pump systems is the excitation force generated by unsteady flow. Due to the asymmetry of the flow field structure, radial forces are inevitably generated during operation. Additionally, a multistage pump uses a balance disc, balance drum, or symmetrical arrangement to eliminate axial force; however, residual axial forces are present in either case. Qian et al. (2022) examined the primary factors influencing the performance of balance drums in multistage pumps using large eddy simulation, proposing a new dual-spiral balance drum design. Cui et al. (2022) analyzed the unsteady flow and fluid-induced vibration forces within multistage centrifugal pumps via large eddy simulation (LES). They found that employing the symmetrical arrangement of the impeller can reduce the axial force to a certain extent, while a symmetrical double tongue distribution significantly lowers radial force and vibration. Abdelouahab et al. (2020) conducted a computational investigation on mechanical properties induced by liquid flow within a multistage pump, simultaneously analyzing the influence of the mechanical characteristics on stress and strain. Tan et al. (2015) studied the impact of the outlet angle of the guide vane on pump performance and discovered that reducing the guide vane exit angle did not alter the fluctuation frequency of the radial force but could somewhat decrease the pulsation amplitude. Cui et al. (2018) obtained the relationship between radial force and vibration by analyzing the fluctuation characteristics of the radial force in a double-volute multistage pump. Kang et al. (2019) investigated the variation in the radial force and its influencing factors, finding that fluctuations in radial force result from non-uniform pressure distribution and pressure variations within the flow field. The above studies mainly focus on design operating conditions. However, there is insufficient research on the relationship between unstable flow and the

Table 1 Parameters of the multistage centrifugal pump

Parameter	Value
Flow rate Q_d/m³/h	350
Head H/m	2200
Rotational speed n/(r/min)	2980
Outlet diameter D_2/mm	375
Blades number Z	7
Number of positive guide vanes	6
Number of anti-guide vanes	6

mechanical characteristics of multistage pumps at high and low flow conditions.

In summary, research on multistage pumps includes optimization design, instability analysis, and mechanical performance but focuses mainly on the rated conditions. However, there is currently limited research on the BB5 series self-balancing multi-stage pumps. Specifically, studies on the differences in flow field and dynamic stability between the low-pressure inlet section and the high-pressure outlet section under various operating conditions have not been reported. Therefore, in this research, the dynamic stability of the self-balancing multistage pump (BB5) was investigated. By analyzing the flow field characteristics and mechanical characteristics of each impeller of the pump, the differences in the dynamic properties of different segments were revealed. These research results can provide a reference for optimizing self-balancing multistage pumps and improving operation stability.

2. COMPUTATIONAL MODELS AND METHODS

2.1 Experimental Model

In this paper, the object of study is a 12-stage self-balancing multistage pump. The structural parameters are shown in Table 1.

Figure 1(a) illustrates the structure of the model pump. Self-balancing multistage pumps using a symmetrical arrangement of impeller combined with thrust bearings to balance axial forces. During operation, the axial force generated in the inlet section is directed to the right, whereas the axial force generated in the outlet section is directed to the left. The directions of these axial forces are opposite, allowing the cancellation of the majority of the axial force. However, due to the gradual increase in pressure, the total axial force produced by the outlet section of the self-balancing multistage pump is larger. This results in a residual axial force directed toward the high-pressure section, which is typically borne by the thrust bearing located in the outlet section.

To reduce the calculation error, the calculation domain adopts full basin modeling, and the fluid domain includes the following: the inlet, inlet extension section, various stages of impellers, various stages of guide vanes, low-pressure outlet section, low-pressure and high-pressure transition section, high-pressure inlet section, pump outlet section, and clearance between the front and rear port rings of each stage, as shown in Fig. 1(b) and 1(c).
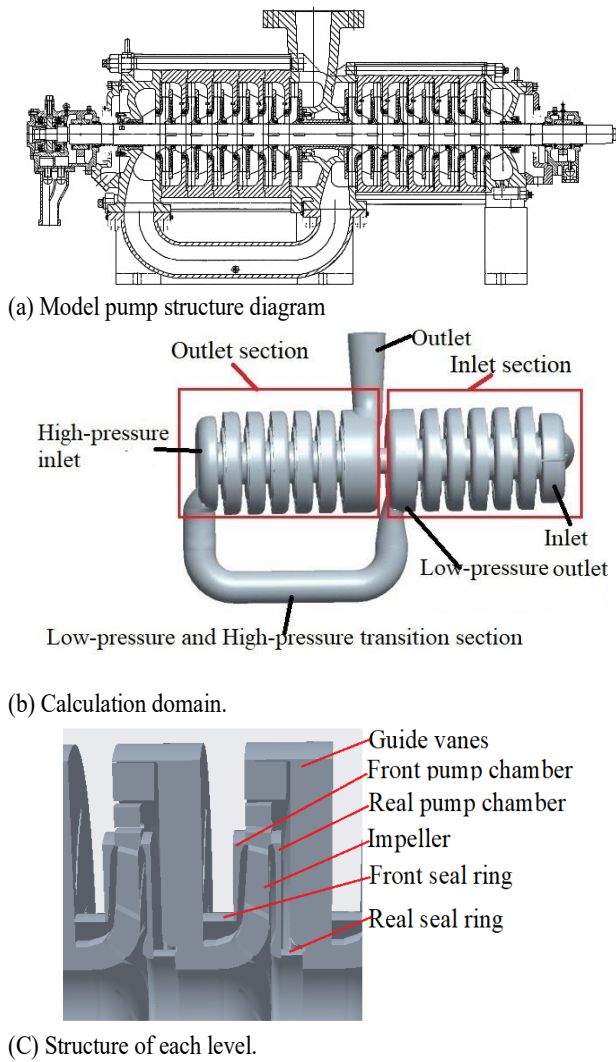
(a) Model pump structure diagram

(b) Calculation domain.

(C) Structure of each level.

Fig. 1 Model calculations

(a) Full flow technology grid.

(b) Grid system of internal components.

Fig. 2 Grid of the model

Fig. 3 Mesh Independence Validation

2.2 Experimental Model

Considering the complexity of the geometric shape of the model pump, unstructured and structured meshes are combined for grid partitioning. Owing to the small size of the front and rear mouth rings, a structural mesh was used to facilitate control over the mesh quality and quantity. Because the size difference between the seal ring clearance and the front and rear pump chambers and guide vanes is large, to solve the mesh transition problem among these structures, some of the water bodies in the pump chambers and guide vanes are integrated with the seal ring to generate a mesh. The grid size is adjusted by setting structural grid nodes. Local mesh refinement was conducted across the corresponding coupling surfaces of the front and rear pump chambers and guide vanes, thereby reducing the difference in the mesh sizes of the coupling surfaces and minimizing the negative impact of the interface on the simulation accuracy. The remaining fluid domains were divided into unstructured tetrahedral grids, as depicted in Fig. 2.

2.3 Verification of Grid Independence

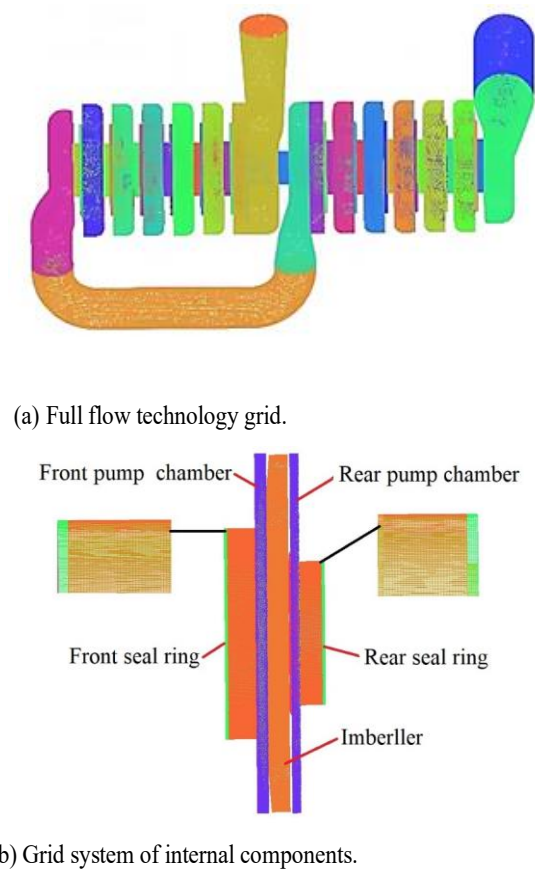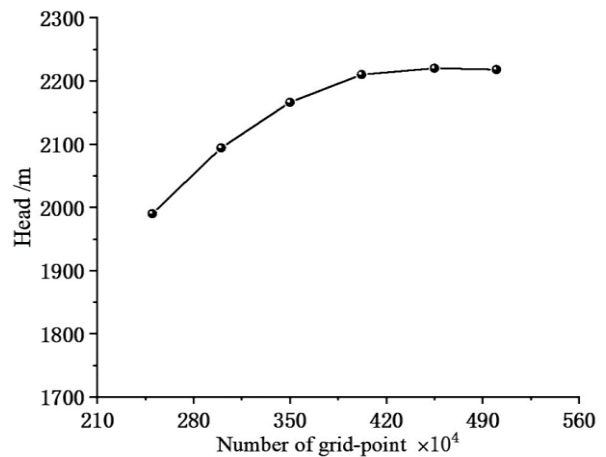Figure 3 shows the relationship curve between the head and the total mesh number of the model pump. A total of 6 grid schemes were numerically calculated, and the corresponding head values were obtained. The head value gradually becomes relatively stable with the increase of grids number, and the head calculation values corresponding to Scheme 5 and Scheme 6 become extremely close. Considering the computing power of the computer, the grid number in scheme 5 is chosen as the reference grid number for numerical calculation in this research. The number of grids is approximately 46 million.

2.4 Numerical Method

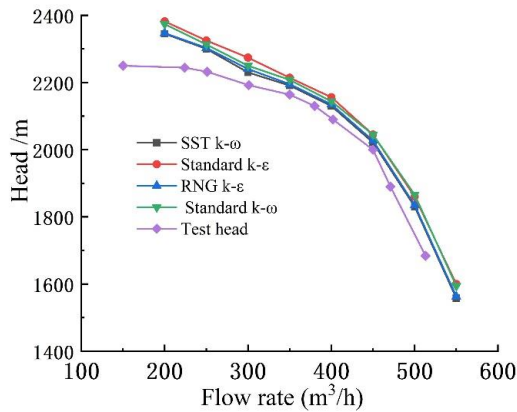Figure 4 shows the variation trends of the calculated and test values of the pump head using the standard k-ε

Fig. 4 Calculation results of different turbulence models

Fig. 5 Experimental system

Fig. 6 Performance curves

model, RNG k-ε model, standard k-ω model, and SST k-ω model.

It can be seen that the numerical calculation results are slightly larger than the experimental values. This is mainly because mechanical friction losses and external leakage losses were not considered in the numerical calculation. At the same time, the highly distorted structure of the centrifugal pump blade causes a high strain rate and a large degree of streamline curvature in the internal flow channel of the impeller. Moreover, different turbulence models handle this kind of flow differently. The calculation results of the RNG k-ε model and the SST k-ω model are close to the experimental results and slightly superior to those of other turbulence models. However, the SST turbulence model combines the advantages of the k-ω and the k-ε model. It has good stability in numerical calculations and can handle complex flow conditions, such as separated flow and recirculation (Zhou et al., 2018; Qian et al., 2022; Zhou et al., 2023). Therefore, the SST turbulence model is adopted in numeric computations. The calculation software used is ANSYS CFX. The inlet is set as the speed inlet. Considering that the flow has fully developed, the outlet is set as a free outflow. When the steady-state calculations between the dynamic and static interfaces are performed, a "frozen rotor" connection is used. And the Transient Rotor-Stator approach is employed for transient simulations. The wall conditions are set as no-slip walls. The time step is the duration it takes for the blade to rotate by 2° and is set to 1.11735×10^{-4} s. The iterations within each step are 30, and the maximum residual is set to 10^{-4}. The calculation cycle consists of 5 rotational cycles, and the transient calculation uses the steady-state calculation result as the initial condition. The data from the 5th rotational cycle after stable calculation are selected for analysis.

3 EXPERIMENTAL

3.1 Test Bench

Pump performance testing is conducted using the company's pump production system, and the layout is shown in Fig. 5.
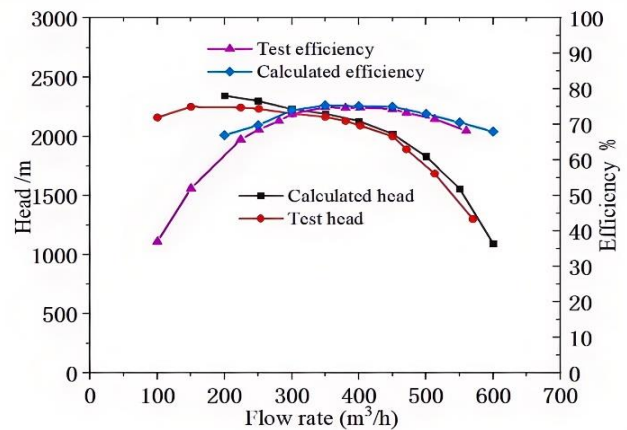
3.2 External Characteristic Verification

As shown in Fig. 6, the calculated and experimental values of the performance curve show similar trends. The numerical calculation results are slightly greater than the experimental values, mainly because the mechanical friction losses in the numerical calculation are neglected. The results indicate a minimal discrepancy between the numerical calculations and the experimental results. Especially at the rated flow rate, the relative error is only 3%.

3.3 Uncertainty Analysis of Numerical Calculation

The uncertainty analysis of CFD simulation results includes two parts: verification and validation. The validation part involves estimating errors and calculating uncertainties in numerical calculations. The confirmation part compares the uncertainty obtained in the verification part with the difference between the numerical calculation result and the test result to determine whether the numerical calculation result is reliable (Deng et al., 2007).

To conduct the uncertainty analysis, three sets of grids with different densities were generated for the model in this paper. The refinement ratio of the grids in the three directions was $\sqrt{2}$, as recommended by ITTC (2002a). The grid sizes of each scheme and the total number of grids in the calculation domain are shown in Table 2.

Table 2 Number and size of three kinds of grids

Scheme	Grid quantity	Head simulation value /m			Head test value		
		$0.8Q_d$	$1.0 Q_d$	$1.2 Q_d$	$0.8 Q_d$	$1.0 Q_d$	$1.2 Q_d$
Coarse mesh	2.8×10^6	2110	2075	1932	2210	2171	2058
Middle grid	3.7×10^6	2211	2174	2050	2210	2171	2058
Refined net	4.6×10^6	2251	2208	2097	2210	2171	2058

Table 3 Verification process

Flow rate	Convergence rate	accuracy order	correction factor	Uncertainty	Corrected uncertainty
	R_H	P_H	C_H	U_{GH}	U_{GHC}
$0.8Q_d$	0.40	2.70	1.55	104	14.3
$1.0 Q_d$	0.34	3.10	1.92	166	17
$1.2 Q_d$	0.40	2.65	1.50	109	13

Table 4 Validation process

Flow rate	U_D (m)	Comparison error (E_H)	Confirm uncertainty (U_{HV})
$0.8Q_d$	44.2	$-41(-1.8\%D_{H0.8Qd})$	$46.4(2.0\%D_{H0.8Qd})$
$1.0 Q_d$	43.42	$-37(-1.7\%D_{H1.0Qd})$	$46.6(2.1\%D_{H1.0Qd})$
$1.2 Q_d$	41.6	$-39(-1.8\%D_{H1.2Qd})$	$43.6(2.1\%D_{H1.2Qd})$

The errors in the CFD calculation process mainly arise from factors such as grid uncertainty and numerical iteration uncertainty. From the calculation experience, when setting the residual convergence criterion for the iterative process to 10^{-4}, it corresponds to at least three orders of magnitude of convergence difference, indicating a stable convergence. The iteration uncertainty is a small quantity and can be ignored (Yang et al.,2010; Zhang et al., 2008). Therefore, the uncertainty of the numerical simulation in this paper mainly depends on the grid factors. Table 3 presents the verification results of the uncertainty of the head under three flow rates. The analysis process was carried out in accordance with the recommended procedures of ITTC (2002b).

Table 4 presents the confirmed results of the uncertainty analysis. In the table, $U_D=2\%D_H$, and D_H represents the head test values under different flow rates. It can be seen that $|E_H| < U_{HV}$. Therefore, the confirmation of the uncertainty U_{HV} under the calculation of flow rate for the three grids has been achieved. This indicates that the grids adopted in this study meet the requirements for calculation accuracy.

4. RESULTS AND ANALYSIS

Considering that the model pump stage is 12 stages. And the effects of the suction section, low-pressure outlet, high-pressure inlet, and pump outlet section on adjacent impellers, we selected levels one, three, six, seven, nine, and twelve for analysis. Among them, stages one, three, and six are located in the inlet section, whereas stages seven, nine, and twelve are located in the outlet section.

4.1. Analysis of the Blade Pressure Load

Figure 7 illustrates the pressure load variation curves for each stage of the impeller blades. The horizontal axis in the figure is the normalized length along the middle streamline of the blade, where 0 represents the blade

mouth and 1 represents the blade outlet. The vertical axis is the pressure coefficient C_p, which is defined as follows:

$$C_p = \frac{p - p_{ver}}{0.5\rho u_2^2} \tag{1}$$

where p and p_{aver} refer to the linear average static pressure of the middle streamline at the blade working surface and the back surface, respectively; u_2 is the circumferential velocity at the impeller outlet; and ρ is the fluid density.

The pressure load coefficients of impeller blades uniformly increase along the middle streamline at the flow rates of $0.8Q_d$, $1.0Q_d$, and $1.2Q_d$, and the change patterns are similar. Under the three operating conditions, three regions of variation in the blade pressure load exist along the relative position of the middle streamline, which are 0 to 0.1, 0.1 to 0.8, and 0.8 to 1.0.

Under three different flow rates, a significant fluctuation in the pressure load coefficient of the low-pressure blade working surface in the range of 0 to 0.1 occurs. This indicates that the flow stability in the inlet area of the working surfaces of the blades in each stage of the inlet section is poor. In the outlet section, the pressure load coefficients both on the work surface and the backing surface are relatively stable without significant fluctuations. At a flow rate of $0.8Q_d$, At a flow rate of $0.8Q_d$, significant differences in the pressure load coefficients of the different blades along the relative length of the blades are observed. The pressure load coefficients of different blades of the same impeller overlap poorly on the corresponding surfaces, and there are differences among them. The results indicate that the symmetry of the flow field structure in each channel of the same impeller is poor, which will cause an imbalance in blade load. At different flow rates, in the normalized length of 0.1 to 0.9, the difference in pressure load coefficients between different blades of each stage of the impeller gradually decreases, especially under the
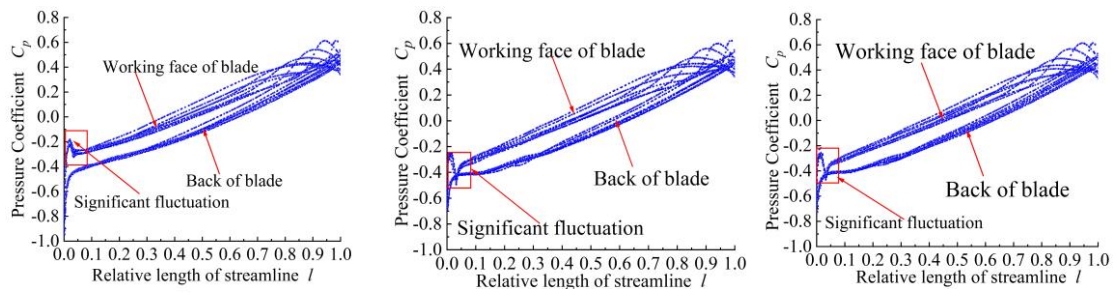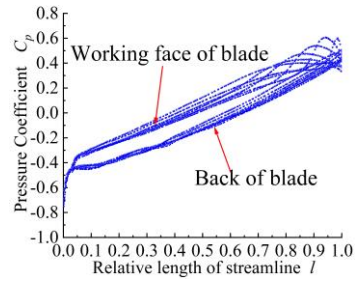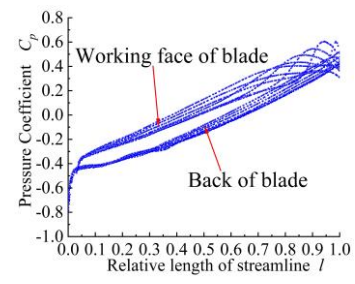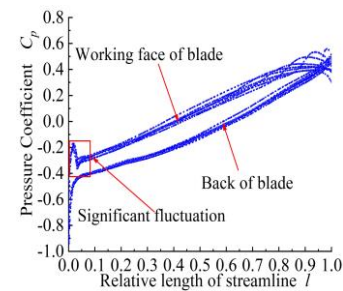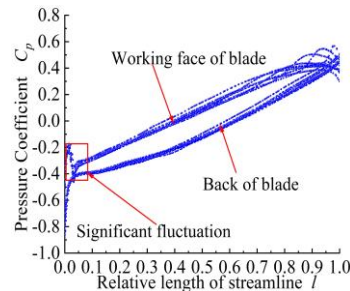
L1   L3   L6
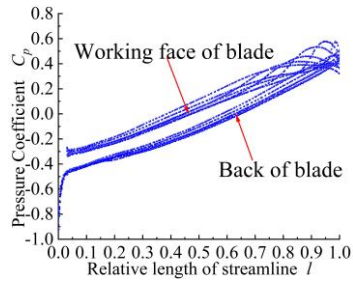
L7   L9   L12

$0.8Q_d$;;;;;;;;
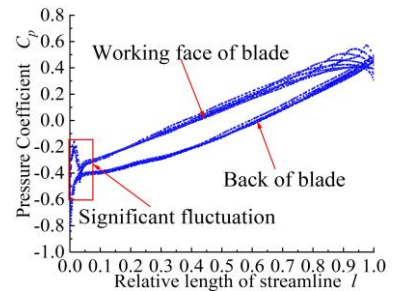
L1   L3   L6
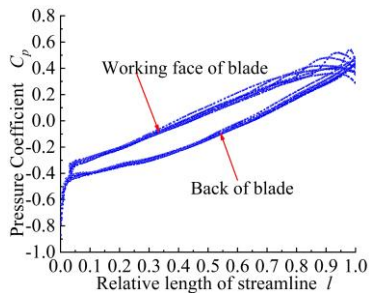
L7   L9   L12

$1.0Q_d$

L1   L3   L6

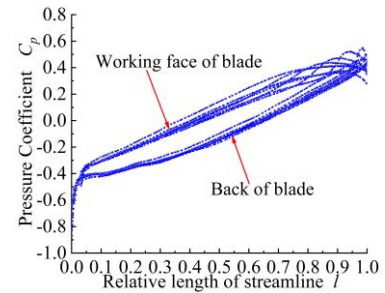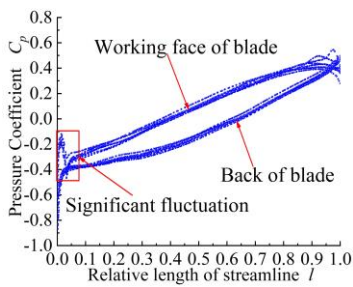L7   L9   L12
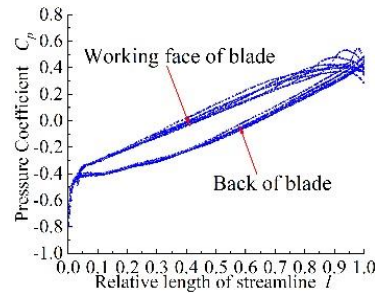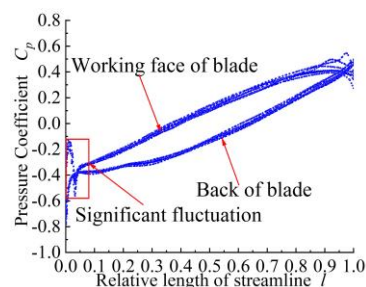
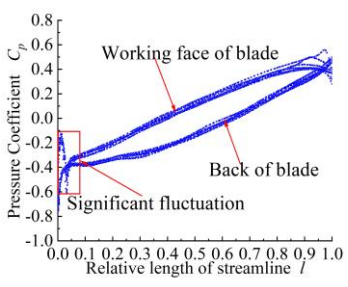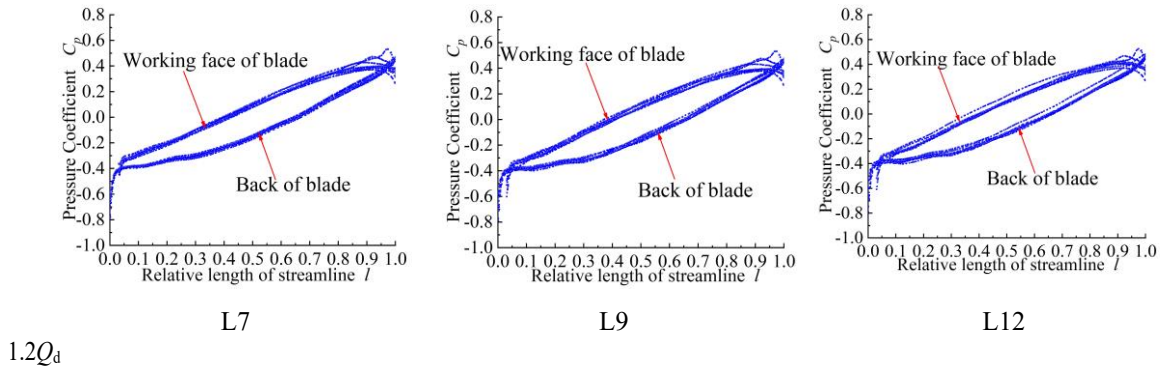1.2Q_d

Fig. 7 Pressure load variation diagram

condition of 1.2Q_d, which tends to be nearly consistent. The symmetry of the blade load has improved.

The pressure load values exhibited significant fluctuations in the range of 0.9 to 1.0, which may be attributed to the wake jet at the blade outlet. As traffic increases, the amplitude of these fluctuations gradually decreases. At a relative distance of 1 from the blade outlet, a tendency for consistency is observed between the pressure load coefficients on both faces.

In summary, certain differences in the distributions and development trends of the blade load coefficients exist between the inlet section and outlet sections of self-balancing multistage pumps. Additionally, the flow rate significantly influences the pressure load coefficient. The variations in the blade loads significantly affect the stability of the self-balancing multistage pump (BB5).

4.2. Analysis of Unsteady-State Characteristics

The unsteady pulsation of the pressure and velocity is the main cause of stability issues in centrifugal pump operation. Therefore, studying the flow field characteristics is the basis for the stability analysis of self-balancing multistage pump. The periodic unsteady flow field variables at the computational node consist of two components: time-averaged variables and periodic variables. For pressure p and flow rate U, they can be defined as follows:

$$p = \bar{p}(n,t) + \tilde{p}(n,t) \tag{2}$$

$$U = \bar{U}(n,t) + \tilde{U}(n,t) \tag{3}$$

where $\bar{U}$ and $\bar{p}$ are the time-averaged components, and $\tilde{U}$ and $\tilde{p}$ are the periodic components. $\bar{U}$ and $\bar{p}$ is defined as follows:

$$\bar{p}(n,t) = \frac{1}{N}\sum_{j=0}^{N-1} p(n,t_0 + j\Delta t) \tag{4}$$

$$\bar{U}(n,t) = \frac{1}{N}\sum_{j=0}^{N-1} U(n,t_0 + j\Delta t) \tag{5}$$

The standard deviation of the periodic components is the pulsation intensity. The circumferential velocity of the impeller outlet was selected for dimensionless processing, and the pressure pulsation intensity (PPI) coefficient and velocity pulsation intensity (VPI) coefficient were

obtained. These values reflect the intensity of the target parameter pulsation within one calculation cycle, regardless of the position of the impeller.

$$C_p^* = \sqrt{\frac{1}{N}\sum_{j=0}^{N-1} \tilde{p}(n,t_0 + j\Delta t)^2} \Big/ 0.5\rho U_2^2 \tag{6}$$

$$C_U^* = \sqrt{\frac{1}{N}\sum_{j=0}^{N-1} \tilde{U}(n,t_0 + j\Delta t)^2} \Big/ U_2 \tag{7}$$

where n represents the grid nodes, N represents the count of samples during a calculation period, and t_0 represents the starting time.

4.2.1. Pressure Fluctuations

Figure 8 indicates the PPI coefficient variation on the cross-section of each stage impeller and the guide vane at flow rates of 0.8Q_d, 1.0Q_d and 1.2Q_d. At the above flow rates, the PPI coefficient inside each stage of the impeller is significantly greater than that inside the guide vanes. The PPI coefficient decreases gradually from inlet to outlet, and the value distribution is uniform. These results indicate that the pressure field inside the guide vane is relatively stable.

With the flow rate decreasing, the PPI coefficient in the impeller gradually increases. The PPI coefficient difference of the same-stage impeller with different flow rates is about 0.1. As the number of stages increases, the PPI coefficient decreases gradually at the same flow rate, indicating relatively weak pressure pulsation inside the high-pressure impeller. This is caused mainly by the increase in the internal pressure of the impeller as the stage increases. The pressure consists of a time-averaged and a periodic component. Overall, the increase in the average pressure component is much greater than that in the periodic component; this leads to a significant reduction in the difference between the two components. Consequently, the pressure pulsation in the outlet section is much smaller than that in the inlet section.

Moreover, the PPI coefficients in the impeller flow channels of each stage exhibit an asymmetric distribution under three different flow rates, and the maximum values occur near the interface between the impeller and the guide vane. This is caused mainly by the interference between the blades and guide vanes. Moreover, asymmetric pressure pulsation with a certain strength
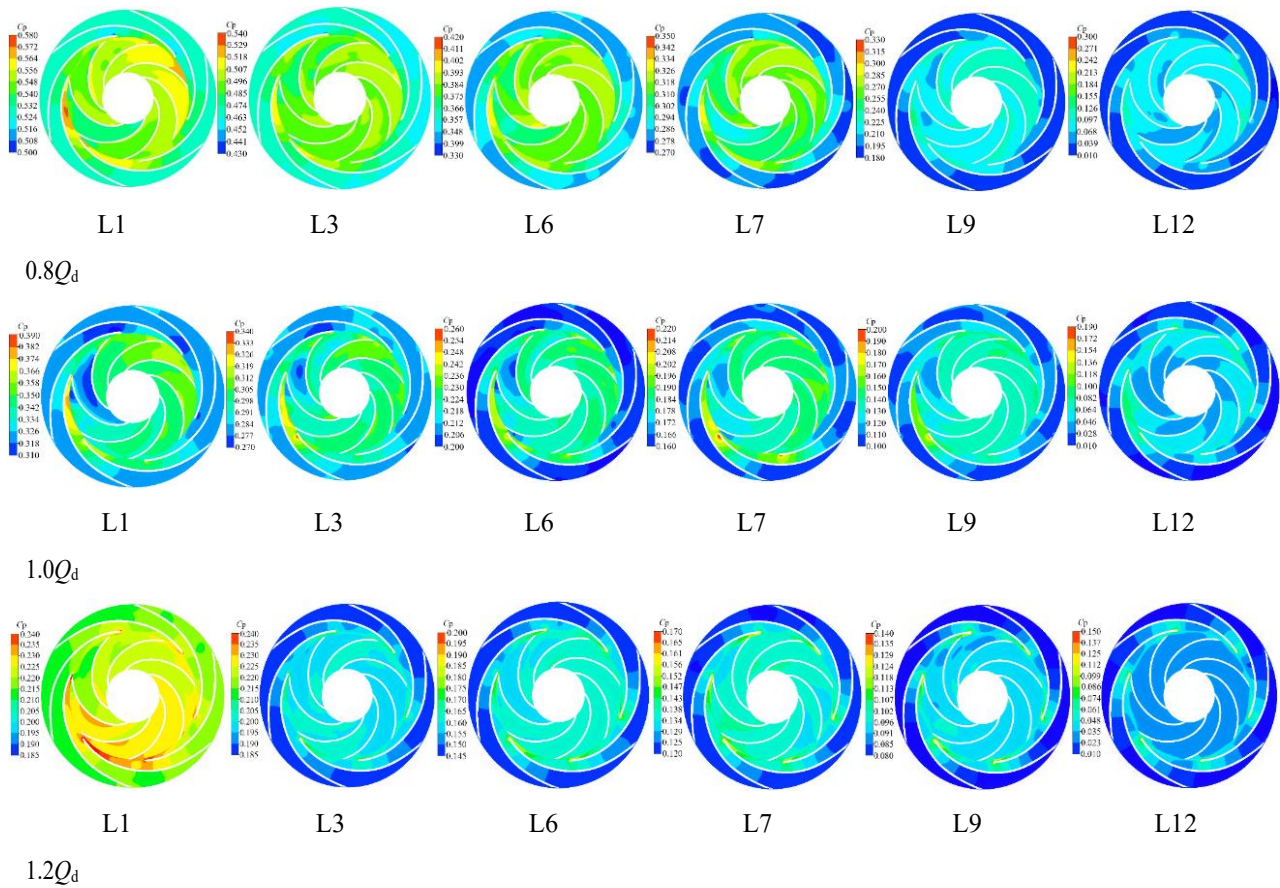
Fig. 8 PPI coefficient distribution

inevitably leads to uneven and asymmetric pressure load changes on the surface of each blade of the same impeller.

Unstable pressure fluctuations affect the structural integrity of centrifugal impellers through various mechanisms, such as fatigue damage, vibration, and resonance. These fluctuations subject the impeller to cyclic loading. As the impeller rotates, changing pressure fields cause stress variations on the blades and other components, leading to fatigue damage. Additionally, pressure pulsation can induce vibration of impellers and other structures. The unstable pressure forces act on the impeller blades, generating dynamic forces that cause the impeller to vibrate. When the pressure fluctuations come close to the natural frequency of the impeller or its components, resonance may occur. Resonance significantly amplifies the vibration amplitude. This leads to a substantial increase in the dynamic stresses on the impeller structure. This not only accelerates the development of fatigue damage but also may lead to the loosening of connections and fasteners, further weakening the structural integrity. The unsteady pressure pulsation within the impeller is a crucial factor in determining the stability of large self-balancing multistage pumps (BB5).

4.2.2. Velocity Fluctuations

Figure 9 shows the VPI coefficient distribution on the cross-section of each stage impeller and the guide vane at flow rates of $0.8Q_d$, $1.0Q_d$ and $1.2Q_d$. As the flow rate increases, the VPI coefficient gradually decreases. A certain intensity of velocity pulsations exists within the guide vanes. The region where the VPI coefficient is greater than 0.038 at $0.8Q_d$ occupies almost all of the flow passage, and the region where the VPI coefficient is

greater than 0.038 at $1.0Q_d$ is distributed at the front of the guide vane flow passage. The VPI coefficient in the guide vane passage at a $1.2Q_d$ flow rate is lower than 0.030, and the intensity of velocity pulsation is reduced.

At the same flow rate, the VPI coefficient within the impeller slightly decreases with the increasing number of stages. The distributions of the high-value regions of the VPI coefficient in each impeller stage are similar and are located mainly in the annular region near the coupling surface of the impeller and guide vane; these results are caused primarily by blade–guide vane interactions. In the region of the back of the blade, the velocity increases due to velocity slip within the impeller passage, whereas vortices tend to form in the flow field, and the changes in vortex strength result in an increase in VPI. Because velocity slip results in a decrease in velocity near the blade working surface, where vortices are not easily formed, the intensity of pressure pulsations at the working surface is weakened. In a self-balanced multistage pump (BB5), the pulsation intensity of internal flow passage components is largely determined by the flow rate.

Based on the above analysis, it can be seen that the pressure and velocity pulsation intensity in the low-pressure inlet section are significantly higher than those in the high-pressure outlet section, indicating that the stability of the inlet section is poor. The high-value areas
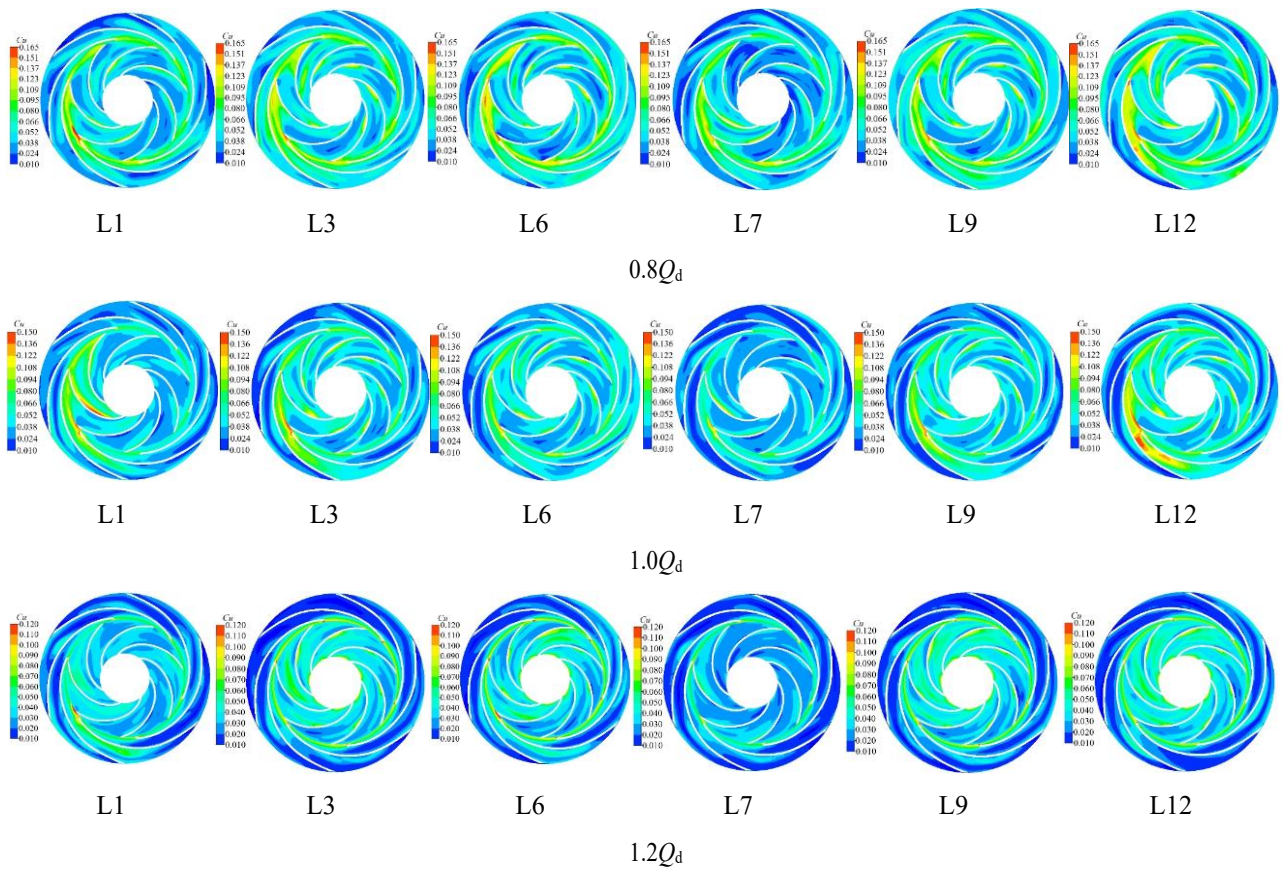
$0.8Q_d$

$1.0Q_d$
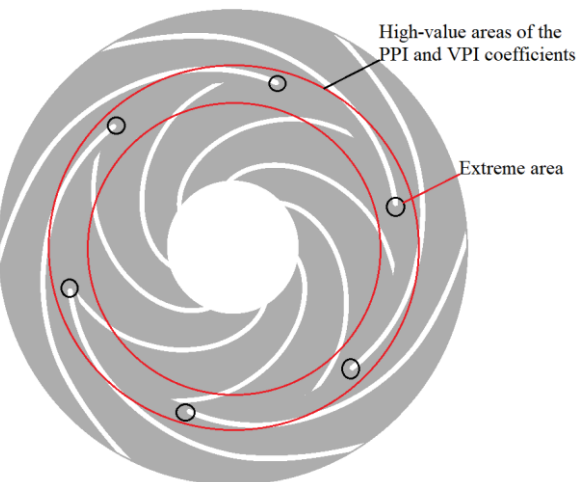

$1.2Q_d$

Fig. 9 VPI coefficient distribution

Fig. 10 PPI and VPI abnormal areas

of PPI and VPI are located at the same position, both in the annular region at the outlet of the impeller and the inlet of the guide vanes. The extreme areas are located at the edge of the guide vane inlet, as shown in Fig. 10. Therefore, in the design process of a self-balancing multistage pump, it is not possible to uniformly use the same impeller for the entire pump as in conventional methods. The inlet low-pressure section and the outlet high-pressure section should be designed specifically. For the impeller in the inlet low-pressure section, in addition to considering the hydraulic performance, the problem of flow field pulsation caused by the interference between the impeller and the guide vanes also needs to be taken into

account.

4.3. Dynamic Characteristic

Radial and axial forces are the most important parameters that determine the stable operation of multistage pumps and play a vital role in bearing life and rotor system stability. The unsteady fluctuation of the pressure and velocity in the pump inevitably affects the magnitude and fluctuation of the radial and axial forces. Because the radial and axial forces of multi-stage pumps are mainly caused by high-pressure liquid in the high-speed rotating impeller, and because the structure of multi-stage pumps is complex, it is challenging to experimentally test the forces acting on the rotating structure. Currently, research in this area primarily relies on numerical calculations. Therefore, this paper conducts a study on the axial and radial forces of self-balancing multi-stage pumps through numerical calculation methods.

4.3.1 Time Domain Analysis of Radial Forces

Figure 11 indicates the time-domain plots of the radial force components during one rotation cycle at the flow rates of $0.8Q_d$, $1.0Q_d$ and $1.2Q_d$. The component forces on each stage of the impeller similarly change during one rotation period at the three flow rates. The radial force component shows evident periodicity, with 6 peaks and 6 troughs. The number of guide vanes of the model pump is 6, which is the main factor determining the fluctuation period of the component forces. The interaction between the impeller and guide vane is the main cause of the component forces in the multistage pump. Moreover, the amplitude of the component forces
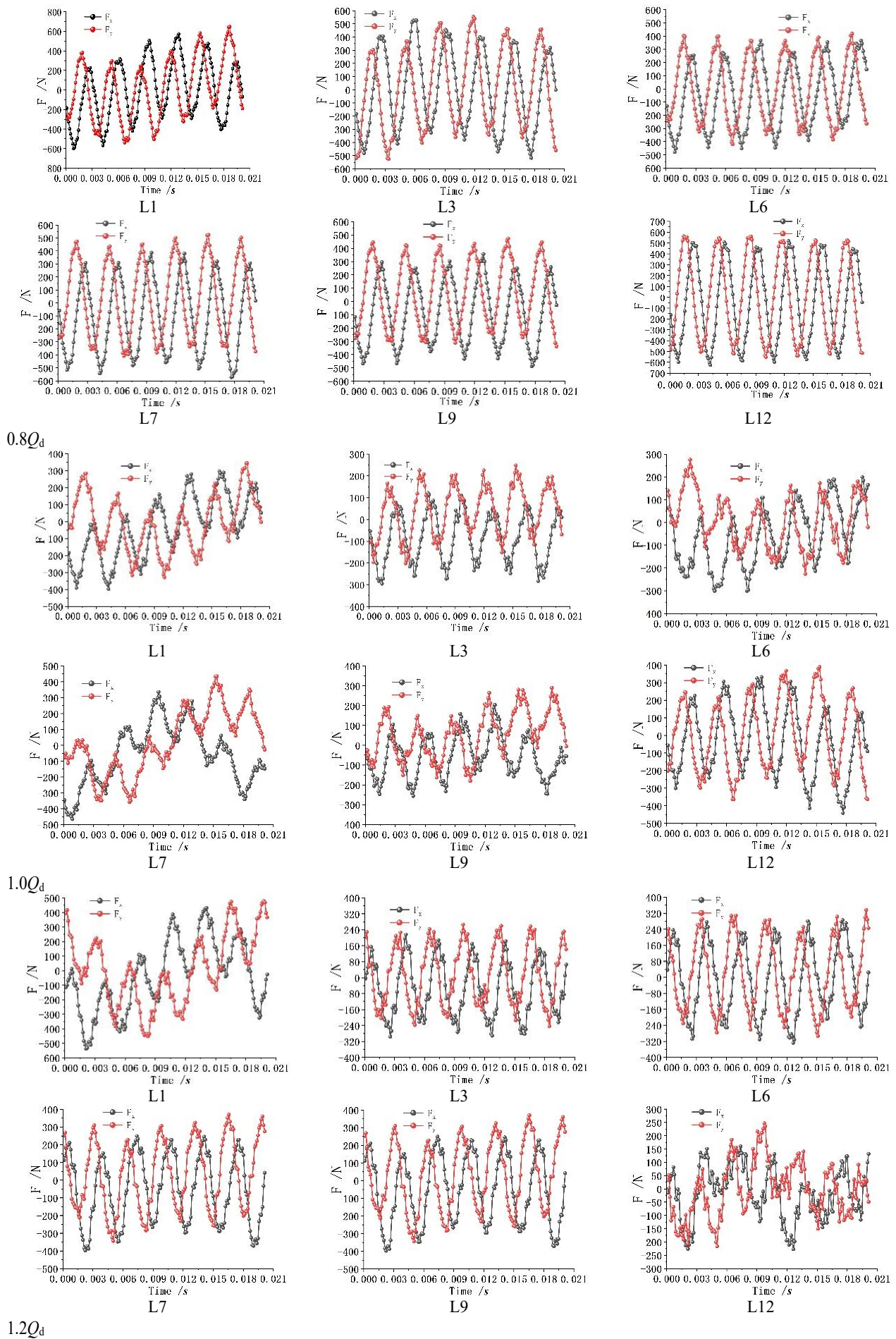
Fig. 11 Time-domain diagram of the radial force components

fluctuates between 500 N and -500 N at $0.8Q_d$. However, at 1.0 Q_d and 1.2 Q_d, the fluctuation range of the component force amplitude narrowed to between 400 N and -400 N. The relationship between the radial force components and flow rate shows that as the flow rate decreases, the component forces increase. The trend of the component forces variation is negatively correlated with the flow rate. However, when the flow rate is greater than $1.0Q_d$, the component forces slightly decrease, and the fluctuation range remains between 200 N and -200 N. The time-domain graph of the component forces is relatively stable at $0.8Q_d$, and the axis of symmetry is the 0 axis. Only slight fluctuations are observed in L1 and L3, and the amplitude at L12 increases. But when the flow rate increases, the time-domain diagram of the component forces on each stage of the impeller is not strictly symmetrical about the 0 axis, and larger fluctuations are observed at L1 and L7. This phenomenon may be due to the impeller of L1 and L7 being close to the inlet of the centrifugal pump and the inlet of the outlet section and being affected by the upstream flow field. However, the L3 and L9 are located in the middle of the multistage pump, with a relatively stable flow field, resulting in a relatively stable time-domain plot of the component forces.

The above analysis indicates that a certain degree of radial force is present in the self-balancing multistage pump. The fluctuation period of each component of radial force is affected by the guide vane blade number. Meanwhile, the radial force component is significantly affected by the change in flow rate, and certain differences in the radial force component of the impellers occur at all levels.

4.3.2 Dynamic-Static Interference Analysis

To analyze the interaction effects between the impeller blades and guide vanes, the vorticity distribution on the middle section of the first-stage impeller was extracted at flow rates of $0.8Q_d$, $1.0Q_d$, and $1.2Q_d$. Additionally, three relative positions of the blade tip and the guide vane inlet within one rotation period were selected for analysis.

As shown in Fig. 12, it can be seen that the vorticity distribution within the middle section of the impeller is similar at three different flow rates. Near the back of the impeller is the main distribution area of the vortex, and the vortex intensity in the blade inlet region is relatively high, approximately 1000 s⁻¹. Meanwhile, there is also a certain intensity of vorticity in the guide vane flow channel, but its value is relatively small. The vortex intensity is the highest in the coupling area between the impeller outlet and the guide vane inlet. During the process of the impeller blade tip sweeping over the guide blade, it can be observed that there is no high-value vorticity distribution between blade 1 and guide vane 1 at time T1. At time T2, the tip of impeller blade 1 swept across the inlet area of guide blade 1, and a high-intensity vorticity appeared in the area between them. At time T3, the tip of the impeller blade 1 leaves guide vane 1, but a high-value vorticity band forms between the tip of blade 1 and the inlet of guide vane 1. Similar situations also occurred between other blades and guide vanes. It can also be observed that

this phenomenon is most evident at low flow rates, and the design flow rate is relatively weaker.

The interaction between the moving blades and the stationary guide vanes results in periodic vorticity pulsations. This leads to periodic changes in the flow field structure, which in turn causes radial force fluctuations.

4.3.3 Spectral Analysis of Radial Force Components

Figure 13 is the spectrum diagram of radial force components acting on each stage of the impeller at $0.8Q_d$, $1.0Q_d$ and $1.2Q_d$. The pump speed is 2980 r/min, and the shaft passing frequency is approximately 49 Hz. In addition, due to the dynamic and static interferences between the guide vanes and impellers of multistage pumps, both the guide vanes and impellers can affect the fluctuations in the radial forces. There are 6 guide vane blades, so the relative blade passing frequency is approximately 298Hz. And there are 7 blades in the impeller, so the blade passing frequency is approximately 343Hz. As shown in Fig 10, at the three flow rates, the radial force component reaches the maximum value when the frequency is 298Hz, but the amplitude is different. At the flow rate of $0.8Q_d$, the amplitude at this frequency is approximately 200 N greater than those at $1.0Q_d$ and $1.2Q_d$. At $0.8Q_d$ and $1.0Q_d$, the amplitude of the component forces of each stage impeller located in the middle is smaller, whereas the amplitude is larger in the first and last stages. The component forces amplitude of the middle-stage impeller at the flow rate of $1.2Q_d$ is greater than that of the first and tail stages. Moreover, at $1.0Q_d$ and $1.2Q_d$, the radial force components exhibit higher amplitudes at the 49 Hz shaft frequency, such as the 7th and 12th stage impellers at flow rate of $1.0Q_d$ and the 1st stage impeller at flow rate of $1.2Q_d$. At $0.8Q_d$, the radial force amplitude at the blade frequency of each stage of the impeller is much greater than that at the shaft frequency, indicating that the radial force of the self-balancing multistage pump at low flow rates mainly depends on the interference between the impeller and the guide vanes. However, at $1.0Q_d$ and 1.2 Q_d, the radial force amplitude at the shaft frequency increases relative to that at the blade frequency, and both act on the entire pump rotor system in combination.

These results show that certain differences exist in the component forces fluctuation process of each multistage pump stage, but the corresponding frequency of the larger value is basically the same. Owing to the unbalanced component forces, the shaft bends and deforms, causing the centerline of the shaft to deviate from the original rotation axis; this results in an uneven load distribution between the shaft and the bearing. On the side of the larger radial force, the pressure on the bearing significantly increases, resulting in intensified wear of the side bearing.

4.3.4. Radial Resultant Force Analysis

Figure 14 shows the variation of the radial resultant force acting on each stage of the impeller at the flow rates of $0.8Q_d$, $1.0Q_d$, and $1.2Q_d$. Each point in the fig represents the instantaneous resultant radial force. Figure 11 shows that the amplitude and direction of the radial resultant
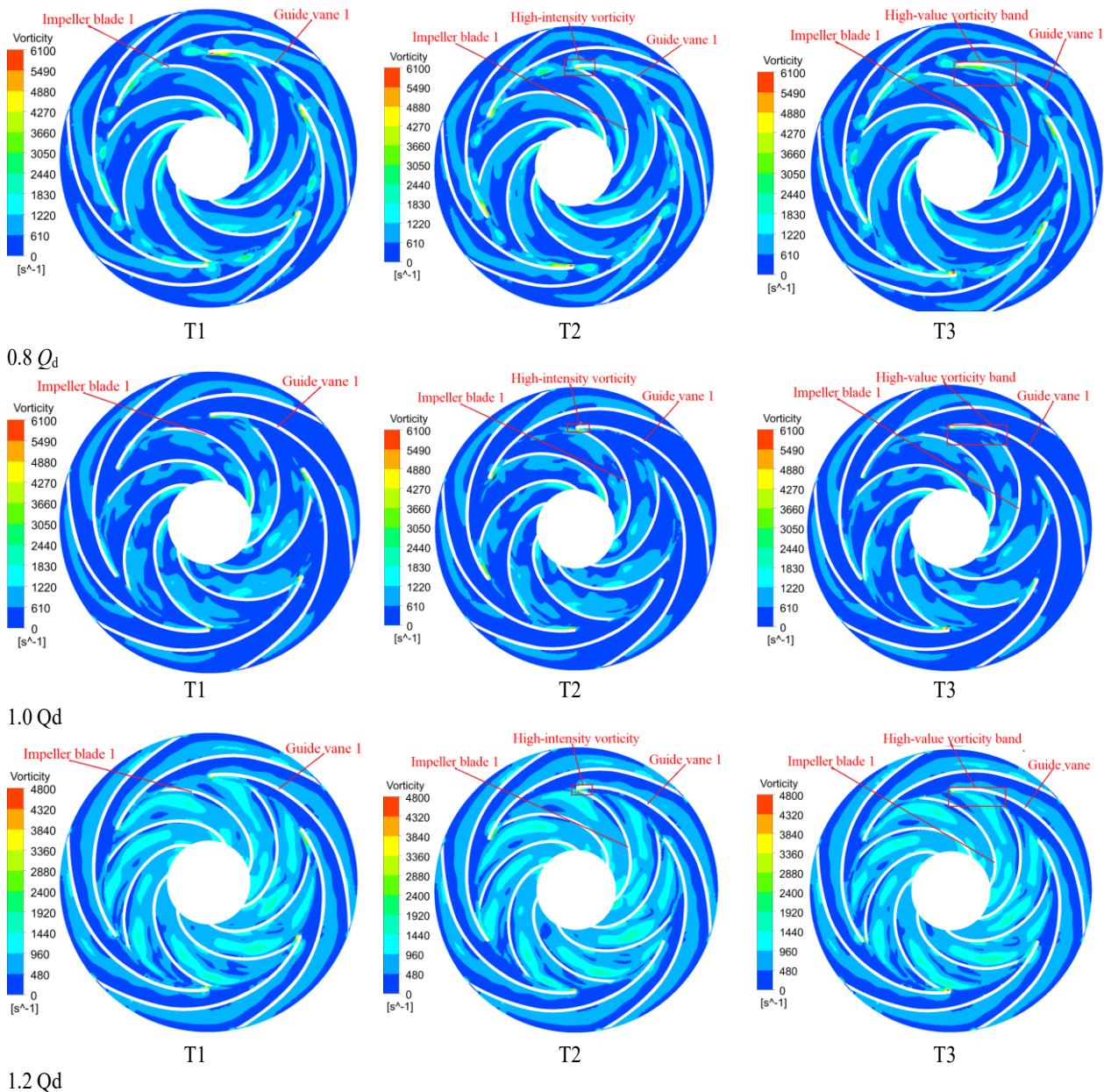
Fig. 12 Cloud diagram of vorticity variation in the middle section of the impeller
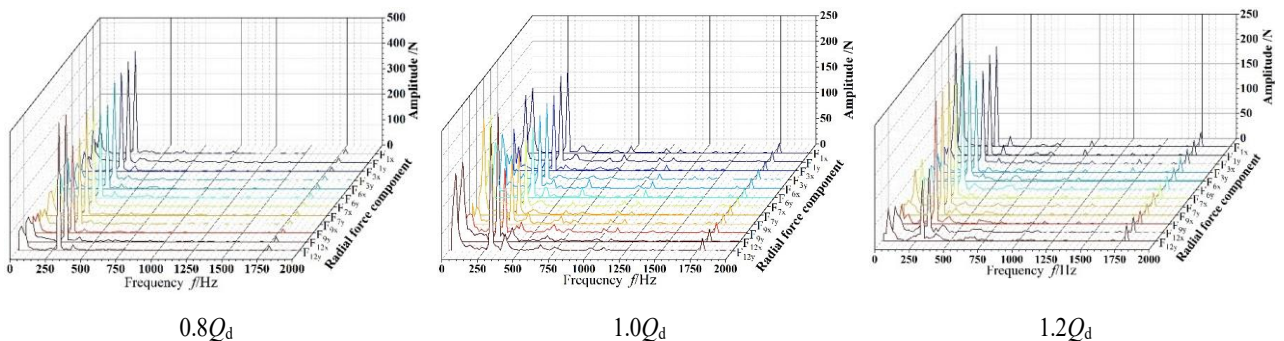

Fig. 13 Spectral diagram of the radial force component

force of each stage of the impeller exhibit periodic changes over time at all flow rates. The distribution shows that a symmetrical center occurs at (0,0), with seven more prominent protrusions and an equal number of leaves.

These results indicate that the change in the radial resultant force is influenced mainly by the rotation effect of the impeller, whereas the resulting radial force is distributed primarily across the seven regions. Moreover,
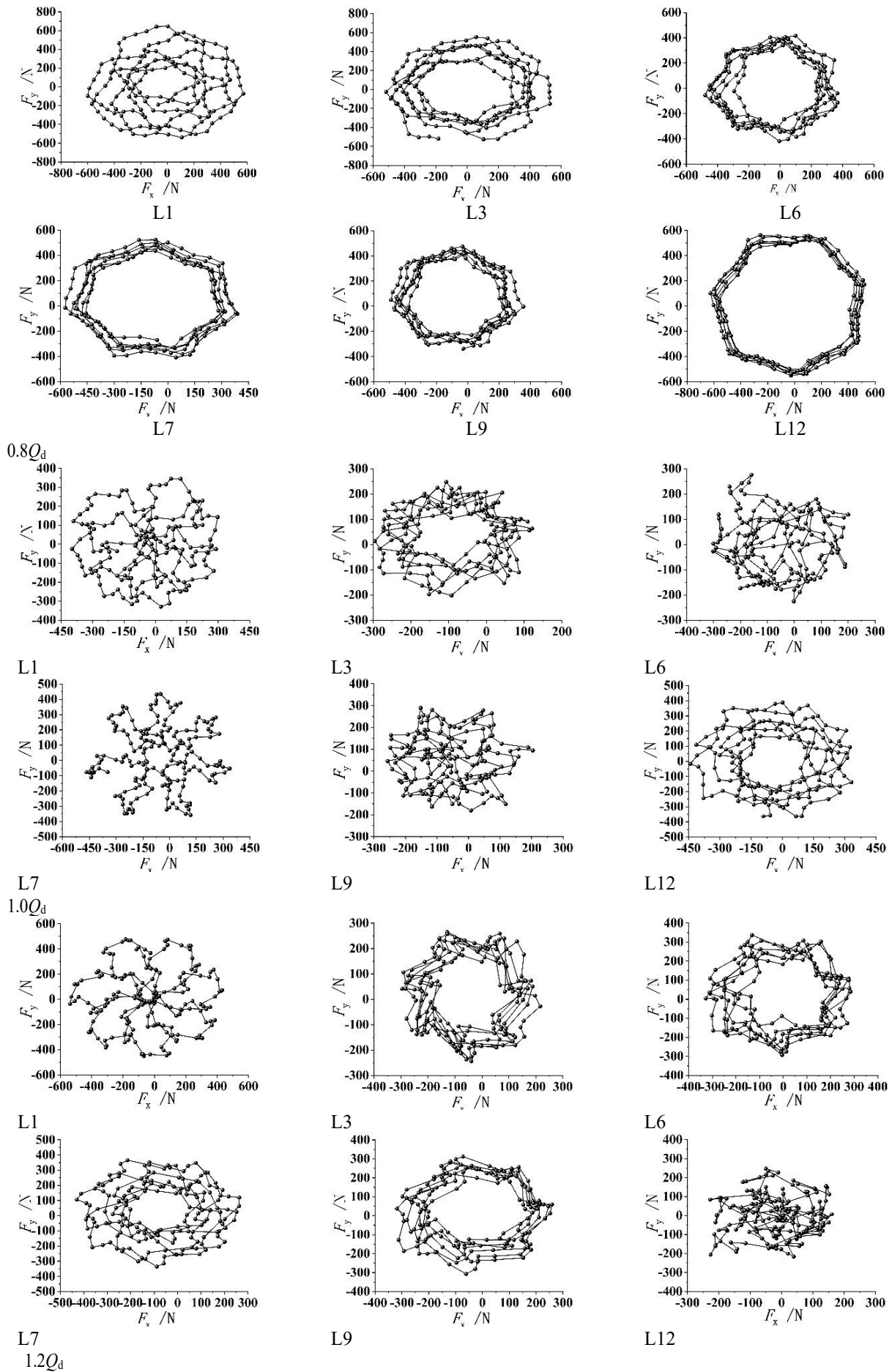
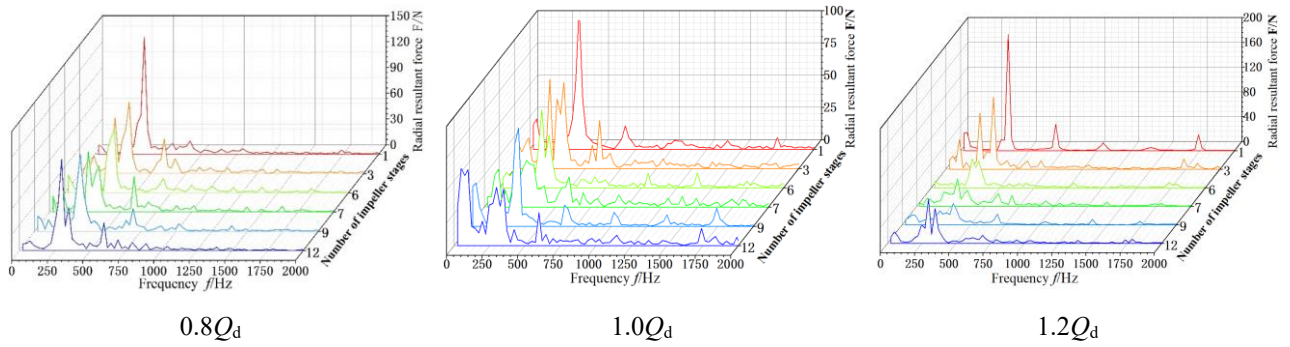**Fig. 14 Radial resultant force diagram**

| 0.8Q_d | 1.0Q_d | 1.2Q_d |

Fig. 15 Frequency spectrum of the radial resultant force
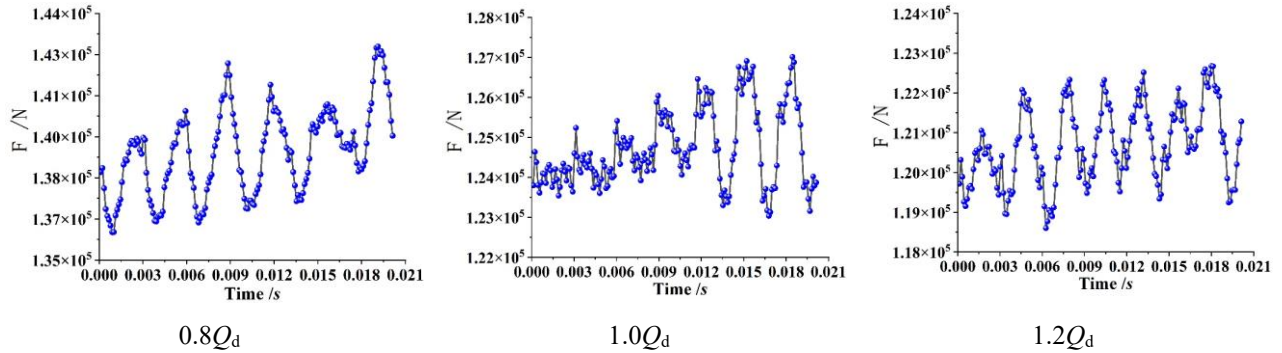

| 0.8Q_d | 1.0Q_d | 1.2Q_d |

Fig. 16 Time-domain diagram of the axial force

based on the similar overall distribution trends, some differences in the radial resultant force distribution of the impeller at all stages at three flow rates are observed. The amplitude of the radial resultant force of each stage impeller varies within the range of 600 N at a flow rate of 0.8 Q_d. The radial resultant force of the first and the third stage e impellers vary considerably and exhibit irregular distribution characteristics. As the number of stages increases, the variation of the radial resultant force tends to become more regular gradually, and the 7-sided feature gradually becomes more prominent. Moreover, the amplitude of the radial resultant force for all stages of the impeller at flow rates of 1.0Q_d and 1.2Q_d fluctuates within a range of 300 N; these results show a significant decrease but lack regularity. The aforementioned changes in the resultant radial force are consistent with the variations in the radial force component spectra shown in Fig. 13. At 0.8Q_d, the amplitude near the blade frequency is much greater than at the shaft frequency, resulting in a relatively regular distribution of the resultant radial force. However, at 1.0 Q_d and 1.2 Q_d, due to the increased proportion of the amplitude of the radial force components at the shaft frequency, the regularity of the distribution of the resultant radial force deteriorates.

The working process of the multistage pump reveals that the impeller of each level generates a certain amount of radial force. This resultant radial force significantly increases at low-flow conditions, while at high-flow rates, the radial force remains relatively low. The distribution of the radial resultant force of each stage impeller is not strictly symmetrical, and the eccentric distribution of the radial resultant force will lead to vibration in the pump rotor system, which may adversely affect the stability of the rotor system operation.

4.3.5. Spectral Analysis of the Radial Resultant Force

Figure 15 shows the frequency spectrum of the radial resultant force on the impeller at the flow rates of 0.8Q_d, 1.0Q_d, and 1.2Q_d. The diagram shows that the radial resultant force reaches its maximum at the frequency of 300Hz and its lower-order harmonic. These results align with the spectral characteristics of the component force. Moreover, a notable distinction in the radial resultant force of each impeller is observed at the three flow rates, and the larger amplitude value appears at the first stage impeller.

But at the flow rates of 0.8Q_d and 1.0Q_d, nearly no difference is observed in the amplitude of the combined force of the other impellers at the frequency of 300Hz. However, at the flow rate of 1.2Q_d, the amplitude decreases to a certain extent as the number of stages increases. Significant differences are observed in the dynamic characteristics of the inlet and outlet sections of the large self-balancing multistage pump (BB5). The stability of the inlet section is not as good as that of the outlet section. This corresponds to the results shown in Fig. 8 and Fig. 9.

4.3.6. Time-Domain Analysis of the Axial Force

Figure 16 shows the variation of the axial force vectors during a rotation cycle at the flow rates of 0.8Q_d, 1.0Q_d, and 1.2Q_d. The axial force direction remains the same at different flow rates. These results indicate that the self-balancing multistage pump cannot fully balance the axial force and still has some residual axial force in a clear direction. This occurs because although the axial forces generated by the outlet and inlet sections of the self-balancing multistage pump are in opposite directions, the axial force generated by the outlet section is greater than
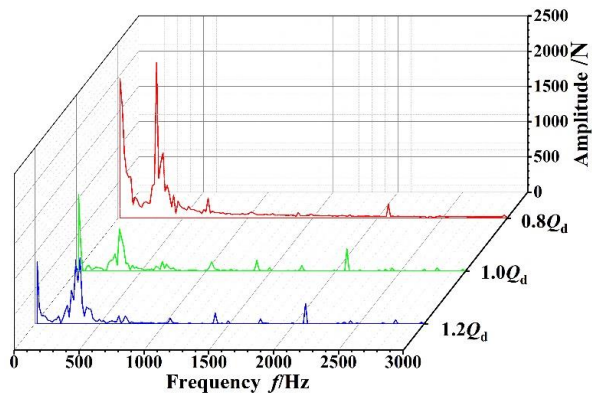
Fig. 17 Frequency spectrum of the Axial force

that generated by the inlet section, resulting in residual axial forces. Moreover, the fluctuations in the residual axial force exhibit a certain periodicity, showing the seven peaks. This may be also related to the interference between the impeller and guide vanes. It is evident that at different flow rates, the maximum amplitude of the axial force also has certain differences. The maximum amplitude of the axial force reaches approximately 1.43×10^5N at $0.8Q_d$, and at flow rates of $1.0Q_d$ and $1.2Q_d$ are approximately 1.26×10^5N and 1.22×10^5N, respectively. As the flow rate decreases, the axial force increases significantly. However, at large flow rates, only a relatively small decrease in the axial force is observed with increasing flow rate. Moreover, the fluctuation of the residual axial force does not follow a regular periodic waveform but rather exhibits certain oscillation characteristics, and these characteristics are related to the unsteady pulsation inside each impeller stage.

4.3.7. Spectral Analysis of Analysis of the Axial Force

Figure 17 shows the frequency spectrum of the axial force at the flow rates of $0.8Q_d$, $1.0Q_d$, and $1.2Q_d$. The axial force spectrum at the flow rates exhibits relatively simple characteristics, and only significant amplitudes appear at a blade passing frequency of 300 Hz and a shaft passing frequency of 49 Hz. The maximum amplitude at the $0.8Q_d$ flow rate reaches 1800 N, whereas at the $1.0Q_d$ and $1.2Q_d$ flow rates, the maximum amplitudes are 1000 N and 800 N, respectively. The axial force increases with the decrease in flow rate. Thus, self-balancing multistage pumps always generate axial forces at a certain frequency under different flow rates rather than stable axial forces. To address fluctuations in the axial force, special designs for either the sliding bearing structure or lubrication system are needed. In terms of the bearing structure, multioil wedge bearings can be used; this design forms stable oil films under different axial force conditions, enhancing the load capacity and stability of the bearing. With respect to the lubrication system, selecting an appropriate viscosity for the lubricating oil is crucial. A viscosity that is too high increases the friction resistance, whereas a viscosity that is too low makes the formation of stable oil films difficult. For the lubrication supply, pressure-fed or recirculating systems need to be employed to ensure that the bearing receives sufficient lubricating oil even during axial force fluctuations to maintain the optimal lubrication conditions.

5. CONCLUSION

In this study, the unsteady flow field and dynamic characteristics inside a 12-stage self-balancing multistage pump (BB5) are investigated using numerical simulation, and the unsteady and mechanical characteristics of the impeller flow field are obtained. The conclusions are as follows:

(1) The pressure loads on the working surfaces and back surfaces of different blades of the same impeller are different. However, as the flow increases, the difference gradually decreases. The pressure loads on the working surfaces and back surfaces of the different blades of each impeller stage nearly overlap at a flow rate of $1.2Q_d$. These results indicate that the uneven force on the blades of each stage of the impeller is strong under low flow rates. The pressure loads on the blade surface in the inlet and outlet regions of the impeller show a certain degree of fluctuation at the three flow rates. In the inlet section, significant fluctuations in pressure in the inlet area of the blade working face occur. In the outlet section, the pressure changes in the inlet area of the working face are relatively stable. The inlet flow conditions of the impeller blades at all levels in the inlet section are worse than those in the outlet section.

(2) A positive correlation exists between pressure, velocity pulsation intensity and flow rate. At the same flow rate, a substantial and notable difference in the pressure pulsation intensity between the inlet and outlet sections is observed. As the number of stages increases, the PPI gradually decreases, and it becomes significantly weaker in the outlet section. The difference in the intensity of velocity pulsation is minimal, and the significant changes are mainly focused on the back of the blade and the annular area between the blade and the guide vane. This phenomenon is caused primarily by the interference between the blades and guide vanes.

(3) The radial force component shows periodic fluctuations at various flow rates. Within a computational cycle, the fluctuation period matches the number of guide vane blades, and the interference between the impeller and guide vanes is the main cause of the radial force generation. Within a rotation cycle, the fluctuation period is equal to the number of guide vane blades, and the interference between the guide vanes and the impeller is the main cause of radial force generation. The frequency spectrum diagram shows that the radial force component has a greater amplitude at a frequency of 300 Hz when the blades pass through and at a relative frequency of 350 Hz when the guide vanes pass through. These results indicate that the number of impeller and guide vane blades are the main factors affecting the fluctuation of the radial force component. The radial force is obviously affected by the flow rate. At a large flow rate, the radial force component is significantly larger compared to the rated and low flow rates.

(4) At the flow rates of $0.8Q_d$, $1.0Q_d$, and $1.2Q_d$, the axial force is not constant, and a certain degree of fluctuation exists. The axial force amplitudes at the three flow rates are approximately 1.43×10^5, 1.26×10^5, and 1.22×10^5. These values show a tendency to increase with

decreasing flow rate. The increase is significant when there is little traffic. The main frequency of axial force variation is 300 Hz, corresponding to the relative passage frequency of guide vanes, and 49 Hz is the axial frequency.

CONFLICT OF INTEREST

We declare that we do not have any commercial or associative interest that represents a conflict of interest unrelated to the work submitted.

AUTHORS CONTRIBUTION

Wensheng Ma: Conceived the innovative points of the study and Provided financial support. **Dongwei Wang:** Writing–original draft and Formal analysis. **Yibin Li:** Data curation. **Rui Cao:** Offered technical support. **Youchao Yang:** Software.

REFERENCES

Abdelouahab, M. A., Ngoma, G. D., Erchiqui, F., & Kabeya, P. (2020). *Numerical study of the axial and radial forces, the stresses and the strains in a high pressure multistage centrifugal pump.* International Conference on Simulation and Modeling Methodologies, Technologies and Applications. 181-188. https://doi.org/10.5220/0009783001810188.

Al Tobi, M. A. S., Bevan, G., Ramachandran, K. P., Wallace, P., & Harrison, D. (2017). Experimental set-up for investigation of fault diagnosis of a centrifugal pump. *International Journal of Mechanical and Mechatronics Engineering, 11*(3), 481-485.

Bai, L., Zhou, L., Jiang, X., Pang, Q., & Ye, D. (2019). Vibration in a multistage centrifugal pump under varied conditions. *Shock and Vibration, 2019*(1), 2057031. https://doi.org/10.1155/2019/2057031

Cui, B., Li, X., Rao, K., Jia, X., & Nie, X. (2018). Analysis of unsteady radial forces of multistage centrifugal pump with double volute. *Engineering Computations, 35*(3) (2018) 1500-1511. https://doi.org/10.1108/EC-12-2016-0445

Cui, B., Zhang, Y., Huang, Y., & Zhu, Z. (2022). Analysis of unsteady flow and fluid exciting forces of multistage centrifugal pump based on actual size. *Proceedings of the Institution of Mechanical Engineers, Part A: Journal of Power and Energy, 236*(1), 21-32. https://doi.org/1177/09576509211023222

Deng, X. G., Zong, W. G., Zhang, L. P., Gao, S. C., & Li., C. (2007). Verification and validation in computational fluid dynamics. *Advance in Mechanics, 37*(2), 279–288. (in Chinese).

Isametova, M., & Abilezova, G. (2022). *Study of the influence of the design of a centrifugal wheel on the pressure characteristics of a multistage pump.* MATEC Web of Conferences. EDP Sciences, 366, 01006. https://doi.org/10.1051/matecconf/202236601006.

ITTC (2002a). ITTC QM Procedure, Uncertainty analysis in CFD verification and validation ethodology and procedures. 7.5-03-01-01.

ITTC (2002b). ITTC QM Procedure, Uncertainty analysis in CFD, examples forresistance and flow. 7.5-03-02-01.

Jiang, W., Pei, J., Wang, W., & Yuan, S. (2021). *Optimization for first stage of multistage pump based on response surface methodology.* IOP Conference Series: Earth and Environmental Science. IOP Publishing, 627(1), 012017. https://doi.org/10.1088/1755-1315/627/1/012017

Kang, Y., Liu, S., Zou, W., & Hu, X. (2019). Numerical investigation on pressure pulsation characteristics and radial force of a deep-sea electric lifting pump at Off-design conditions. *Shock and Vibration, 2019*(1), 4707039. https://doi.org/10.1155/2019/4707039

Kim, D. S., Mamatov, S., Jeon, S. G., & Park, W. G. (2017). A study of the performance of a radial diffuser for a multistage high-pressure pump. *Journal of Mechanical Science and Technology, 31*, 1693-1700. https://doi.org/10.1007/s12206-017-0317-8

Li, W., Jiang, X., Pang, Q., Zhou, L., & Wang, W. (2016). Numerical simulation and performance analysis of a four-stage centrifugal pump. *Advances in Mechanical Engineering, 8*(10), 1687814016673756. https://doi.org/10.1177/1687814016673756

Lu, Z., Wang, C., Qiu, N., Shi, W., Jiang, X., Feng, Q., & Cao, W. (2018). Experimental study on the unsteady performance of the multistage centrifugal pump. *Journal of the Brazilian Society of Mechanical Sciences and Engineering, 40*, 1-10. https://doi.org/10.1007/s40430-018-1157-x

Milovančević, M., Nikolić. V., Petkovic, D. L., Vracar, E., Tomic, Veg. N., & Jović, S. (2018). Vibration analyzing in horizontal pumping aggregate by soft computing. *Measurement, 125*, 454-462. https://doi.org/10.1016/j.measurement.2018.04.100,2-s2.0-850467060 53.

Peng, G., Hong, S., Chang, H., Zhang, Z., & Fan, F. (2021). Optimization design of multistage pump impeller based on response surface methodology. *Journal of Theoretical and Applied Mechanics, 59*(4), 595-609. https://doi.org/10.15632/jtam-pl/141939

Qian, C., Luo, X., Yang, C., & Wang, B. (2022). Calculation and verification of balance force of multistage pump balance drum. *Proceedings of the Institution of Mechanical Engineers, Part C: Journal of Mechanical Engineering Science, 236*(1), 153-164. https://doi.org/

Qian, C., Yang, L. H., Qi, Z. P., Yang, C. X., & Niu, C. H.

(2022). Mechanism analysis of double helical balance drum to improve axial force of multistage pump. *Modern Physics Letters B, 36*(35), 2250185. https://doi.org/10.1142/S0217984922501846

Tan, M., Guo, B., Liu, H., Wu, X., & Wang, K. (2015). Investigation of radial force and hydraulic performance in a centrifugal pump with different guide vane outlet angle. *Journal of Vibroengineering, 17*(6), 3247-3260. https://www.extrica.com/article/16075

Wang, S., Yang, J., & Xu, G. (2023). Influence of positive guide vane geometric parameters on the head-flow curve of the multistage pump as turbine. *Processes, 11*(12), 3393. https://doi.org/10.3390/pr11123393

Wang, Z., Lu, C., Qiu, N., Shi, W., Jiang, X., Feng, Q., & Cao, W. (2018). Experimental study on the unsteady performance of the multistage centrifugal pump. *Journal of the Brazilian Society of Mechanical Sciences and Engineering, 40*(5), 1-10. https://doi.org/10.1007/ s40430- 018-1157-x, 2-s2.0-85046084 116.n

Wu, T., Wu, D., Gao, S., Song, Y., Ren, Y., & Mou, J. (2023). Multi-objective optimization and loss analysis of multistage centrifugal pumps, *Energy, 284* (2023), 128638. https://doi.org/10.1016/j.energy.2023.128638

Yang, R. Y., Shen, H. C., & Yao, H. Z. (2010). Uncertain analysis of CFD simulation on the open-wa-ter performance of the propeller. *Journal of Ship Mechanics, 14*(2), 472-480.

Yuan, S. Q., Shi, W. D., & Liu, H. L. (2014). *Theory and Technology of Pump.* China Machine Press, Beijing.

Zhang, N., Shen, H. C., & Yao, H. Z. (2008). Uncertain analysis in CFD for resistance and flow field. *Journal of Ship Mechanics, 12*(2), 211-224. https://doi.org/10.3969/j.issn.1007-7294.2008.02.007.

Zhang, L., Wang, D., Yang, G., Pan, Q., Shi, W., & Zhao, R. (2024). Optimization of hydraulic efficiency and internal flow characteristics of a multi-stage pump using RBF neural network. *Water, 16*(11), 1488. https://doi.org/10.3390/w16111488

Zhang, S., Li, X., & Zhu, Z. (2018). Numerical simulation of cryogenic cavitating flow by an extended transport-based cavitation model with thermal effects. *Cryogenics, 92*, 98-104. https://doi.org/10.1016/j.cryogenics.2018.04.008

Zhang, Y., Liu, J., Yang, X., Li, H., Chen, S., Lv, W., Xu,W., Zheng J & Wang, D. (2022). Vibration analysis of a high-pressure multistage centrifugal pump. *Scientific Reports, 12*(1) 20293. https://doi.org/10.1038/s41598-022-22605-2

Zhao, J., Pei, J., Yuan, J., & Wang, W. (2023). Structural optimization of multistage centrifugal pump via computational fluid dynamics and machine learning method. *Journal of Computational Design and Engineering, 10*(3), 1204-1218. https://doi.org/10.1093/jcde/qwad045

Zhou, L., Bai, L., Li, W., Shi, W., & Wang, C. (2018). PIV validation of different turbulence models used for numerical simulation of a centrifugal pump diffuser. *Engineering Computations, 35*(1), 2-17. https://doi.org/ 10.1108 /EC-07-2016-0251.

Zhou, R. Z., Liu, H. L., Hua, R. N., Dong, L., Ooi, K. T., Dai, C., & Hu, S. Y. (2023). Induced noise of impeller stuck and passive rotation state in multi-stage pump without power drive under natural flow conditions. *Journal of Hydrodynamics, 35*(5), 1008-1026. https://doi.org/10.1007/s42241-023-0068-1.